Actinic characterization of extreme ultraviolet bump-type phase defects

Kenneth A. Goldberg[a] and Iacopo Mochi
Center for X-Ray Optics, Lawrence Berkeley National Laboratory, Berkeley, California 94720

(Received 24 June 2011; accepted 22 September 2011; published 25 October 2011)

Multilayer blank defects in extreme ultraviolet (EUV) lithography photomasks continue to be among the highest concerns impeding commercialization. The SEMATECH Berkeley Actinic Inspection Tool (AIT), an all-EUV, high-magnification microscope, is routinely used to investigate mask defects, including native and programmed defects on mask blanks. So-called *phase defects*, created by buried substrate bumps and pits, formed within or below the EUV-reflective multilayer coating, cause phase-shifts in the reflected light field. These small disturbances are difficult to detect, yet they can create critical defects in patterns arranged above them. The authors report the through-focus measurement of programmed defects with a range of sizes reaching below the optical resolution of the AIT, and below the detection capabilities of advanced deep ultraviolet mask blank inspection tools. Consistent with previous measurements of native phase defects, we find that the observed phase and intensity changes are much smaller than predicted by a simple phase-change model based on the measured top-surface profile. Through simulation, we investigate the dependence of defect detectability on the illumination partial coherence. © *2011 American Vacuum Society*. [DOI: 10.1116/1.3653257]

I. INTRODUCTION

The importance of extreme ultraviolet (EUV) mask defects has driven ongoing research on their effects for more than 15 years. Current measurable defect density levels for multilayer (ML) blanks are orders of magnitude higher than they must be for defect-free mask fabrication.[1] Compounding the problem, state of the art commercial blank inspection tools may not be capable of detecting the smaller sizes of so-called *printable defects* that affect pattern critical dimensions (CDs) on the printed resist wafer. These sizes may be between 10 and 50 nm FWHM, and 1–2 nm high depending strongly on the design CDs and the illumination properties. Despite known gaps in our collective understanding of the nature and impact of defects, few experimental tools are now capable of providing direct, aerial-image measurements of real defects, without printing in photoresist.[2]

Of particular concern is the class of defects known as *phase defects,* which are caused by pits, bumps, trapped particles, and other imperfections in the mask substrate, or in the EUV-reflective multilayer-coating itself. Defects of this category may be only tens of nm wide and 1 nm tall, at the surface of the multilayer coating, yet they can cause significant disruption in the reflected EUV-light field, especially when imaged out of focus. Due to the complexity of the reflective multilayer coating as an optical system, one cannot yet reliably predict the impact of a defect on the printed pattern based on the top-surface defect shape. While EUV-light reaches deeply into the multilayer stack and is sensitive to disruptions well below the surface, light from deep ultraviolet (DUV) inspection tools penetrates only the top few layers, making it potentially less sensitive to small but relevant defects.[3] This difference in the physical response serves as a primary motivation of the need for *actinic* inspection and imaging of EUV masks (i.e., using EUV light) for defect analysis and disposition.

The Actinic Inspection Tool (AIT) is one of the few tools currently available to perform EUV aerial image measurements of known phase defects.[2] Other tools include the extreme ultraviolet microscope (EUVM), developed by the University of Hyogo,[4] and the EUV imaging system at Aachen.[5] The EUVM has demonstrated the ability to image patterned phase-shifting features, including lines and point-like defects. It relies on an EUV Schwarzschild objective combined with an x-ray zooming tube to provide a variable two-stage magnification. Ultimately, its aberration-limited resolution is not as high as that of the AIT. The Aachen tool utilizes a combination of reflective optics and diffractive (zoneplate) optics to provide moderately high resolution. It is now under development and published results include only low-resolution features. In contrast to the others, the AIT uses a single, high-magnification zoneplate lens to produce magnification ratios on the order of 900 with direct EUV imaging; the AIT has demonstrated diffraction-limited performance.[6] The AIT is described in the following text.

To systematically characterize and compare the response of DUV and EUV tools, a test mask containing arrays of phase defects of varying sizes was fabricated from programmed bumps on the substrate.[7] Here, we describe the measured EUV response to these defects, including the characterization of the light-to-dark through-focus behavior characteristic of phase defects. The measured response is compared with a *single-surface approximation* (SSA) model[8] based on the average AFM-measured top-surface profiles of the defects.

In addition to experimental measurements, we present simulations of the important role of illumination partial coherence in defect "detectability." Imaging models predict that the through-focus behavior of the minimum and maximum aerial image intensity varies strongly with the degree

[a]Electronic mail: KAGoldberg@lbl.gov

of partial coherence—at higher σ values, defects become much more difficult to observe.

A. SEMATECH Berkeley AIT

The AIT is a synchrotron-based, high-magnification, EUV mask-imaging microscope.[9,10] A bending magnet beamline at Lawrence Berkeley National Laboratory's Advanced Light Source provides tunable, narrow-band, focused illumination onto an approximately 30-μm wide region of the mask surface with a 6° angle of incidence similar to an EUV scanner. The central wavelength is 13.4 nm, and the illumination bandwidth is set to approximately $\lambda/\Delta\lambda = 1450$ by a plane-grating monochromator. In the AIT, a zoneplate lens positioned in the reflected beam path projects the image of a small region of the mask surface onto an EUV-sensitive charge-coupled device (CCD) camera[11] with approximately 900× magnification. The imaging quality approaches diffraction-limited performance at the central region of the image.[12] The AIT has a user-selectable array of zoneplate lenses with different numerical apertures, to emulate the spatial resolution of various current and future EUV scanners. Mask-side numerical aperture values currently installed in the AIT are {0.0625, 0.08, and 0.0875}, enabling the AIT to emulate {0.25, 0.32, and 0.35} 4× NA, wafer-side imaging.

The mask-imaging performed in this study was conducted using the highest available numerical aperture in the AIT: 0.0875 NA on the mask side (equivalent to 0.35 NA in a 4× scanner). For this NA value, we estimate the partial coherence of the illumination to have a σ value close to 0.15.[9] Images are projected with a linear pixel density of approximately 15 nm per pixel, oversampling the Rayleigh resolution by a factor greater than 6 (note: 0.61 λ/NA = 93.4 nm). For these measurements, a 45 s exposure time was used for these experiments, producing an average photon level of approximately 500 photons per pixel. We measure the CCD camera's inherent background level by recording and averaging three dark images.

Recently, data from a through-focus imaging series in the AIT has been used to reconstruct the amplitude and phase of defects and phase-structures on EUV masks. These measurements are particularly interesting for their potential to improve the predicted response to various defect repair strategies.[13,14]

B. Single-surface approximation (SSA)

The through-focus behavior of phase defects has been studied by several authors,[15–18] in both theory and experiment. Whereas amplitude (absorbing) defects reduce the beam intensity through-focus, phase defects exhibit a characteristic bright-to-dark (or dark-to-bright) intensity transition through-focus that reveals whether a defect behaves like a bump or pit. Images of bump type defects appear bright in the center when the wafer is closer to the imaging lens, and appear dark when the wafer is farther from the lens. In an aerial image microscope, where a CCD camera replaces the wafer, the analogous focal displacements occur with the mask farther or closer to the lens, respectively. Conversely the bright/dark image appearance of pit-type phase defects occurs with the opposite focal displacements.

A simple, but useful framework for understanding defect behavior was proposed by Gullikson *et al.*[8] Known as the single-surface approximation (SSA), the premise of the model is that a plane wave reflected from a defect will acquire a phase change proportional to the top-surface height disturbance. In this way, a defect of height, h, imparts a phase change of $\Delta\square = 2hk$, where the wave number, k, is $2\pi/\lambda$. The SSA model provides a way to simulate the complex aerial image field by carrying the perturbed reflected field through the lens to the image plane.

Earlier work[15,19] has shown that the SSA typically overpredicts the observed intensity and phase changes of small defects, where spatial filtering by the lens reduces the defect's amplitude and apparent phase in the image. Ultimately, a defect's phase comes from its underlying shape and the structure of the multilayer, which is dependent on deposition and growth conditions.[20]

C. Difficulty of evaluating printability based on blank defect measurement

The question of *printability* is central to the discussion of defect size, yet it is difficult to generalize based on measured or modeled intensity and phase changes in open field (i.e., defects on a ML blank). Phase defect printability depends not only on the defect size but also on the relative location to patterns on the mask. For this reason, worst-case scenarios could, in principle, be used to predict the potential severity of measured defects. It may not be possible to create a general predictive model that correlates a defect's maximum intensity change through-focus to its printability in a given pattern. Yet intensity change is a measurable quantity that is useful for characterizing detectability above background noise.

II. BUMP-TYPE PROGRAMMED-DEFECT MASK

Test masks with programmed defect arrays are critical tools for defect characterization and tool development. While it could be argued that naturally occurring, "native" defects are most relevant for real-world studies, the use of well-characterized defect arrays of various types and sizes accelerates learning, provides ensemble statistics, and gives a common test vehicle for the systematic assessment of available inspection tools.

A. Description of the test mask

The programmed-defect array mask was designed to contain eighteen arrays of defects with each array containing 400 defects of the same size: this provides a large sample for reliable statistical analysis. The test mask was fabricated with standard patterning and ML deposition processes. A thin Cr layer containing the defect array was patterned onto the mask substrate and then over-coated with a standard Mo/Si multilayer stack. A description of the preparation of a similar mask is available in Ref. 18.

In the interest of assessing defect printability for patterning 22 nm half-pitch and beyond, only measurements of smaller defects, starting from array 9 are reported in this paper. Figure 1 shows the AIT images of the defects and corresponding sizes [in terms of height and full-width at half-maximum (FWHM)] measured by atomic force microscopy (AFM) on the top surface of the ML stack. In array 9, the bumps appear as 120-nm wide (FWHM) and 1.6-nm tall. Such large defects are easily detectable by DUV inspection tools and EUV imaging. Defects in array 16 are just 43-nm-FWHM and 1.0-nm tall. Such defects are difficult to measure by any tool. The defects in arrays 17 and 18 were too small to be measurable by AFM.

In mask defect inspection, spherical-equivalent volume diameter (SEVD) is a common, linear metric used to describe the size of defects. Several authors, including Stokowski *et al.*,[22] have made the observation that comparing the interaction of light with flat, wide, Gaussian shaped surface defects to a similar interaction with spherical particles of equivalent volume leads to potentially false conclusions. The surface shapes, slopes, and curvatures that dictate scattering and reflection, for example, are significantly different between the two geometries. Nevertheless, we use SEVD as a linear volumetric reference, while noting that caution must be used in a physical defect volume comparison.

III. PROGRAMMED-DEFECT ARRAY MEASUREMENTS

A mask of this type enables straightforward cross-comparison of inspection and imaging results from multiple tools. Large arrays of similar defects make the collection of meaningful detection statistics possible. This is especially true for the high-speed DUV tools, which measure all points on the mask in a relatively short time. The AIT was used only to measure a few defects of each size.

Prior to the EUV measurements, the mask was measured using two state of the art DUV mask inspection tools, as reported Liang *et al.* at the SPIE Photomask (BACUS) meeting in Sept. 2010.[7] When inspected using 266-nm-wavelength light, defects in array 11 (1.5 nm height × 90 nm FWHM, 30 nm SEVD) were detected with 93% capture efficiency. With 193-nm-wavelength light, defects in array 12 (1.4nm height × 80 nm FWHM, 27 nm SEVD) were observed with 92% capture efficiency and no false counts. Below these cutoff sizes, defect detection levels fell sharply.

The AIT measured a total of 23 defects on this mask, through-focus, in arrays 9 through 17. A sampling of the measurements is shown in Fig. 1. The focal-step size used in the experiments is 0.4 μm, equivalent to 25 nm on a wafer in a 4× scanner. Details from every other image are shown in Fig. 1. We observe that the central point undergoes the characteristic bright-to-dark transition for bump-type defects with the mask translating away from the projection lens. It is clear that phase defects produce a higher signal, and hence become more printable, when out of focus.

Figure 2 shows the minimum intensity value for each through-focus series. The trend-line is plotted through the average measured value in each array. We note that defects become increasingly faint in the higher array numbers, but are measurable even in array 17 where the AFM showed a negligible profile. The AIT measurements of the aerial image show that defects from array 16 (1.0 nm height × 43 nm FWHM, 16 nm SEVD) produce a nearly 20% intensity change in a defocused measurement position. The SEVD value could not be measured for array 17, so the abscissa value used here is extrapolated from arrays 13 through 16.

Comparison of these actinic and DUV measurements must be made with consideration of the following. The DUV tools run at relatively high speed, covering an entire mask surface and finding defects with no *a priori* information, in a period from 20 min to 2 h, while the AIT must be carefully driven to the known defect positions for measurement, and

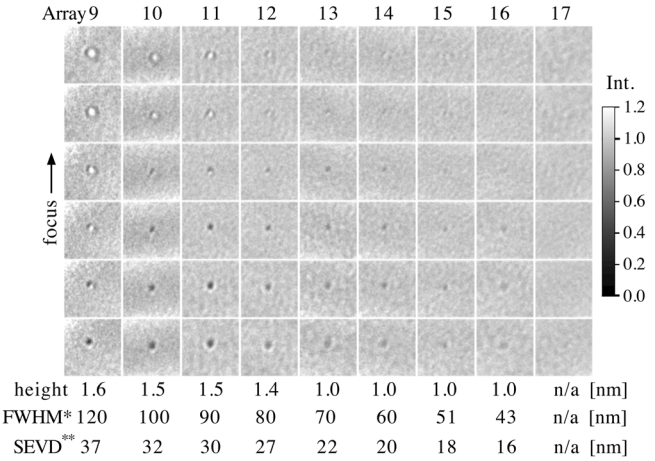

FIG. 1. Representative defect images recorded through-focus, from nine arrays in the programmed defect array. The AFM-measured top-surface sizes are shown for each array. Images are separated by 0.8-μm focal steps (mask side), the equivalent of 50-nm on a wafer scale. Each image is shown in a 1.5-μm square field of view, normalized on a linear intensity grayscale between 0 and 1.2, with the average bright background level set to unity. As a reference, the defect size is also shown as the diameter of a sphere with the volume equivalent to the Gaussian shape of the phase bump. (* denotes the full-width at half-maximum and ** denotes the spherical-equivalent volume diameter.)

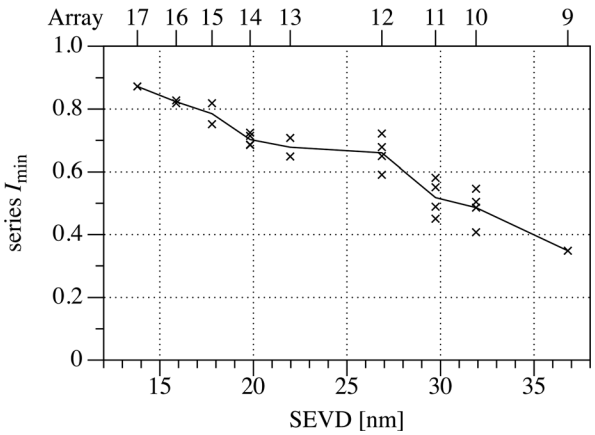

FIG. 2. Minimum normalized intensity values through-focus for all measured defects. The trend line is plotted from the available data, through the average measured value in each array. Note: the un-measured SEVD of array 17 is extrapolated from arrays 13 through 16 values.

through-focus data collection typically requires 20 min per series. This speed difference is not inherent to the discussion of actinic versus DUV (nonactinic) mask inspection, but arises from the current speed limitations of the AIT.

A. Actinic limitations of phase-defect actinic detectability

Speckle, shot-noise, and the finite imaging resolution, are the primary factors limiting the detectability of phase defects in the AIT.

As described by Naulleau[23] and George,[24] speckle arises from *multilayer phase roughness* observed in the relatively high coherence of the AIT illumination ($\sigma \leq 0.2$). Speckle appears as small-scale intensity variations in the EUV images with a RMS magnitude that is typically several percent of the average bright-region intensity. The characteristic minimum size of the speckle pattern is determined by the (NA dependent) resolution of the AIT. We observe that the amplitude of the speckle pattern varies from mask to mask, yet has a characteristic through-focus behavior. The speckle pattern is comprised primarily of phase variations in the aerial image. When imaged in focus, the intensity variation is minimized. Out of focus, and in the presence of aberrations (from misalignment or from field-dependent variation), the intensity amplitude increases slightly and the spatial-frequency content of the pattern changes in a manner that visibly increases the mean size of the speckles.[24]

Shot noise is significant in AIT measurements. Following Poisson statistics, with a bright intensity level of 500 photons per pixel, the RMS intensity variation from shot-noise is expected to be 4.5%.

In the subject data, we observe a bright-region RMS variation close to 7.5%. Assuming the speckle and shot-noise contributions are uncorrelated, their individual magnitudes add in quadrature. Under this assumption, the contribution from speckle alone is 6.0%.

Identifying phase defects within the speckle and shot-noise thus requires intensity changes of approximately 15% to achieve 2σ confidence, and 22.5% for 3σ confidence. For reference, an image detail region with 1.5 μm square area contains an area equal to approximately 258 resolution elements at the AIT's highest NA (0.0875 on the mask side). Achieving a 1-in-258 confidence level for defect detection requires a measured intensity change greater than 2.89σ, or 21.6%. Since shot noise occupies all spatial frequencies equally, but the apparent sizes of the defects are limited by the resolution of the lens, these numbers may overstate the requirements, and the defects may, in fact, be somewhat easier to detect through proper image filtering. The defects in arrays 16 and 17 have smaller intensity differences than this level. Detecting them by eye, or with a signal-processing algorithm must rely on their ring-shaped pattern and bright-to-dark through-focus behavior, in addition to the single-image intensity change alone.

Even if there were more light, speckle has a strong influence on the detectability of phase defects. In essence, the speckle itself is a low-level background of random phase defects.

Beyond the role of speckle and shot noise, the limited resolution of an imaging lens also plays a role in defect detectability. Defects below the spatial resolution of the lens scatter light outside of the pupil, thus reducing the apparent intensity amplitude changes caused by the defect.

B. Phase measurements

We have recently reported the calculation of complex aerial image intensities from a through-focus image series collected with the AIT.[19,23] An iterative phase reconstruction technique searches for a self-consistent complex field solution for the best-focus image. The input information for such phase reconstruction includes a series of seven consecutive image details through-focus, plus the known numerical aperture of the imaging lens, and the assumptions that the imaging performance is of diffraction-limited quality in the vicinity of the defect, and the illumination is fully coherent. The resulting calculations reveal the phase distribution created by the measured defects in the aerial images.

The measured phases are shown in Fig. 3, where the measured phase changes are converted to an effective surface height change (using the optical path difference, $h = \Delta\Phi/2k$), and the AFM-measured heights are plotted for each defect array. The small-sized defects of primary interest are below the spatial resolution of the imaging lens; thus, spatial filtering reduces the peak phase amplitude in the image, relative to the phase change at the mask.

Uncertainty in the phase measurement arises from two primary sources of measurement error: shot noise and image-series misalignment. Simulations of Gaussian phase defects performed with 500 photos per measurement pixel, show that shot noise contributes less than 0.02 rads of phase uncertainty (equivalent to 0.02-nm height uncertainty, considering the factor of two path length change upon reflection).[19] Image misalignment within the series is a more subtle cause of phase-measurement errors. The algorithm

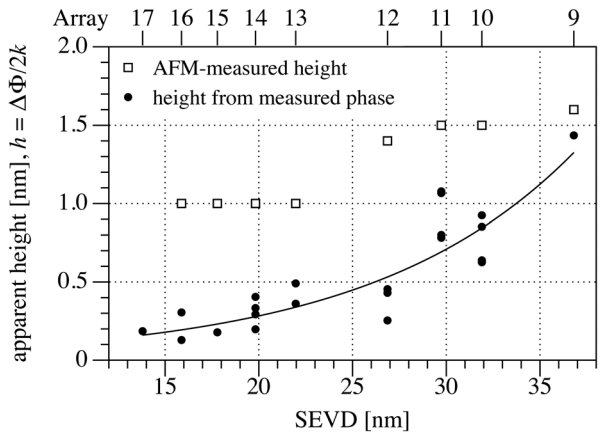

FIG. 3. Calculated peak phase change values in the best focus images of the measured defects are converted to an effective height change based on the optical path difference. Also shown are the AFM-measured heights of the defects in each array. For defects smaller than the imaging resolution, the curves diverge significantly due to the spatial filtering of the objective lens.

used to reconstruct the phase assumes that changes in the intensity distribution arise from the phase of the image and the propagating light field through-focus; thus, unintentional image misalignments are interpreted as phase. We estimate the image alignment accuracy to be within 0.1 pixel (1.5 nm) RMS,[19] which is less than 2% of the Rayleigh resolution at 0.0875 mask-side NA, and less than 3.5% of the FWHM of the smallest measurable defects in this study. The measured-phase error caused by placement uncertainty depends on the image features (and slope) and is difficult to generalize. The topic is the subject of ongoing research.

IV. EFFECT OF ILLUMINATION PARTIAL COHERENCE ON DEFECT DETECTION

To optimize imaging performance in a scanner, various off-axis illumination conditions are selected to suit specific resist patterning requirements. Accordingly, it is important to analyze the variation of through-focus intensity from phase defects as a function of the illumination partial coherence. To our knowledge, previously published investigations of isolated EUV phase defects' through-focus behavior has been limited to the assumption of coherent illumination. However, analysis of the expected through-focus intensity variation from phase defects shows that the system response is highly sensitive to the illumination partial coherence. Modeling, based on the sum-of-coherent-sources (SOCS) solution to the Hopkins formulation of partially coherent imaging[25,26] shows that as the partial coherence σ value increases upward from zero (i.e. fully coherent), the amplitudes of the intensity minima and maxima decrease.

The plots in Figs. 4 and 5 show the modeled central intensity values through-focus for three defects. Using the top-surface defect shape and the SSA to model the reflected light field, the partial-coherent imaging cases are calculated using SOCS. At higher σ values, the characteristic out-of-focus intensity changes become blurred, and thereby smaller. In focus, there is little change in the central intensity, yet the large amplitude excursions occur outside of best focus, where the effects of partial coherence are most strongly felt.

Interestingly, our model predicts that for the smallest defects and largest σ values, there is no through-focus maximum intensity value above 1.0. The origin of this behavior is that at large angles of illumination, light from these small defects is scattered out of the pupil, thereby reducing the central intensity for all focal positions. In the defocus positions where bright intensity maxima can occur, the large range of illumination angles substantially blurs the defect image. This effect also has implications for the ML phase roughness. We have stated previously that the physical observation of small phase defects requires separation of the defect signal from a nonuniform background caused by speckle and shot-noise. With partially coherent illumination acting to reduce the through-focus intensity changes of phase defects, we can infer that a similar effect would reduce the intensity variation from speckle. This complex topic deserves further investigation to determine if there may be an optimal partial coherence condition to maximize the phase defect detection SNR for a given range of defect sizes.

V. SUMMARY

Phase defects are among the most vexing issue facing EUV lithography in mass production. By the nature of their small size and their characteristic through-focus behavior—becoming bright or dark on opposite sides of focus—they can be difficult to detect at sizes that potentially cause printable defects.

Using an EUV aerial image microscope to study a programmed defect mask with a buried bump-type defect pattern, we have measured defects with top-surface sizes below 1-nm tall and 43-nm FWHM (15 nm SEVD). These defects cause potentially critical intensity and phase changes in the aerial image, but fall below the detection sensitivity of current state-of-the-art DUV inspection tools, which have been reported to have a 93% capture rate for defects of 27 nm SEVD.[7]

We observe that with bright-field actinic imaging, detection sensitivities are affected by the presence of speckle, due to multilayer phase roughness (a property that varies from

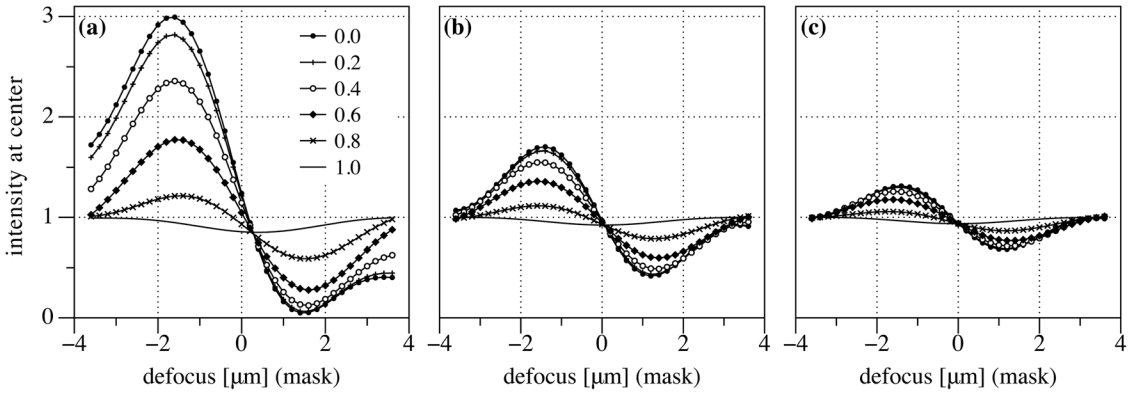

FIG. 4. Central image intensity values calculated through-focus using the SSA for three defect sizes: (a) array 9, 1.6 ht. × 120 FWHM; (b) array 13, 1.3 ht. × 70 FWHM; and (c) array 16, 1.0 ht. × 43 FWHM. Within each plot the different curves correspond to partial coherence σ values varying from 0 (fully coherent) to 1. As σ increases, the out-of-focus intensity changes are reduced. The SSA typically over-predicts the observed intensity changes, but serves as a useful tool for understanding defect behavior.

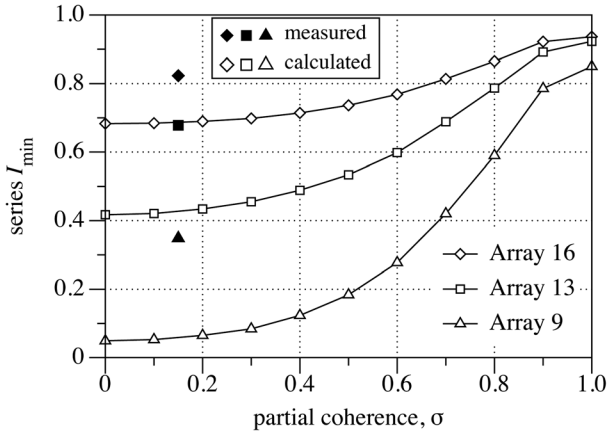

FIG. 5. Central image-intensity minimum values within the through-focus series illustrated in Fig. 4, calculated for σ values from 0 to 1. Open symbols represent calculated values for defects in arrays 9, 13, and 16. Corresponding solid symbols are the measured average intensity minimum values from the same arrays, using an estimated σ value of 0.15.

mask to mask). Because the phase defects' peak intensity changes (maximum and minimum) occur out of focus, the intensity changes in the images are particularly sensitive to the illumination partial coherence. Aerial image simulations predict that isolated defect detection sensitivity will fall with increasing σ values, yet we can also infer that the intensity variation from speckle will decrease in a similar manner; the multilayer phase roughness that creates the speckle may be envisioned as a random array of phase defects, subject to the same detection physics.

In the absence of speckle, actinic phase-defect detection efficiency ultimately depends on the intensity change a defect produces and the detection signal-to-noise ratio. Simulations predict that for the defect sizes calculated here, the intensity minima start to change significantly when σ values go above 0.4. Below that level, detection efficiencies are close to those of coherent illumination.

ACKNOWLEDGMENTS

We wish to thank Ted Liang of Intel for his support in providing the mask, the DUV inspection data, and the impetus for this study. We wish to acknowledge the support of SEMATECH and project leader Hyuk Joo (Harry) Kwon. The AFM measurements of selected phase bumps were provided by Hoya. This work was performed under the auspices of the U.S. Department of Energy by the University of California Lawrence Berkeley National Laboratory under management and operating Contract No. DE-AC02-05CH11231. This work was funded by SEMATECH under Agreement No. LB08005006.

[1]U. Okoroanyanwu, A. Tchikoulaeva, P. Ackmann, O. Wood, B. La Fontaine, K. Bubke, C. Holfeld, J.-H. Peters, S. Kini, S. Watson, I. Lee, B. Mu, P. Lim, S. Raghunathan, C. Boye, Proc. SPIE **7636**, 7636J (2010).
[2]K. A. Goldberg and I. Mochi, J. Vac. Sci. Technol. B **28**(6), C6E1 (2010).
[3]K. A. Goldberg, A. Barty, P. Seidel, K. Edinger, R. Fettig, P. Kearney, H. Han, and O. R. Wood II, Proc. SPIE **6517**, 65170C (2007).
[4]H. Kinoshita, K. Hamamoto, N. Sakaya, M. Hosoya, and T. Watanabe, Jpn. J. Appl. Phys., Part 1 **46**, 6113 (2007).
[5]S. Herbert, A. Maryasov, L. Juschkin, R. Lebert, and K. Bergmann, Proc. SPIE **7545**, 75450O (2010).
[6]I. Mochi, K. A. Goldberg, P. Naulleau, and S. Huh, Proc. SPIE **7271**, 727123 (2009).
[7]T. Liang, SPIE Photomask BACUS Meeting, Monterey, CA, September 15, (2010), (unpublished).
[8]E. M. Gullikson, C. Cerjan, D. G. Stearns, P. B. Mirkirimi, and D. W. Sweeney, J. Vac. Sci. Technol. B **20**(1), 81 (2002).
[9]K. A. Goldberg, I. Mochi, P. P. Naulleau, H.-S. Han, and S. Huh, Proc. SPIE **7122**, 71222E (2008).
[10]K. A. Goldberg, I. Mochi, and S. Huh, Proc. SPIE **7271**, 72713N (2009).
[11]Princeton Instruments, PIXIS-XO CCD camera, see http://www.princetoninstruments.com/products/xraycam/pisx/
[12]I. Mochi, K. A. Goldberg, P. Naulleau, and S. Huh, Proc. SPIE **7271**, 76361A (2009)
[13]D. W. Sweeney and A. K. Ray-Chaudhuri, U.S. patent 6,235,434 (22 May 2001).
[14]M. Waiblinger, K. Kornilov, T. Hofmann, and K. Edinger, Proc. SPIE **7545**, 75450P (2010).
[15]C. H. Clifford, S. Wiraatmadja, T. T. Chan, A. R. Neureuther, K. A. Goldberg, I. Mochi, and T. Liang, J. Vac. Sci. Technol. B **27**, 2888-2893 (2009).
[16]I. Kang, H. Seo, B. Ahn, D. Lee, D. Kim, and S. Huh, Proc. SPIE **7636**, 76361B (2010).
[17]S. Huh, A. Rastegar, S. Wurm, and K. Goldberg, Proc. SPIE **7545**, 75450N (2010).
[18]I. Mochi, K. A. Goldberg, and S. Huh, J. Vac. Sci. Technol. B **28**, C6E11 (2010).
[19]I. Mochi, K. A. Goldberg, R. Xie, P.-Y. Yan, and K. Yamazoe, Proc. SPIE **7969**, 7969X (2011).
[20]C. H. Clifford, "Simulation and compensation methods for EUV lithography masks with buried defects," Ph.D. dissertation (University of California-Berkeley, 1997).
[21]T. Kinoshita, T. Shoki, H. Kobayashi, R. Ohkubo, Y.-I. Usui, M. Hosoya, N. Sakaya, and O. Nagarekawa, SPIE **5256**, 595 (2003).
[22]S. Stokowski, J. Glasser, G. Inderhees, and P. Sankuratri, Proc. SPIE **7636**, 76360Z (2010).
[23]P. P. Naulleau, Appl. Opt. **43**(20), 4025 (2004).
[24]S. A. George, P. P. Naulleau, E. M. Gullikson, I. Mochi, F. Salmassi, K. A. Goldberg, and E. H. Anderson, Proc. SPIE **7969**, 79690E (2011).
[25]R. J. Socha, A. R. Neureuther, J. Vac. Sci. Technol. B **14**(6), 3724 (1996).
[26]R. J. Socha, "Propagation effects of partially coherent light in optical lithography and inspection," Ph.D. dissertation (University of California-Berkeley, 1997).